Thermal expansion of $Sr_xBa_{1-x}Nb_2O_6$ across and above the ferroelectric phase transition

Viviann H. Pedersen[1], Elvia A. Chevez Panduro[1], Weicheng Hua[1], Marcus G. Michaelsen[1], Dmitry Chernyshov[2], Julian Walker[1], Tor Grande[1] and Mari-Ann Einarsrud[1]

[1] Department of Materials Science and Engineering, NTNU Norwegian University of Science and Technology, Trondheim, Norway

[2]Swiss-Norwegian Beamlines, European Synchrotron Radiation Facility, Grenoble, France

Abstract

Lead-free $Sr_xBa_{1-x}Nb_2O_6$(SBN) is of interest due to flexible chemistry, ferroelectric behavior, and electro-optic properties. The thermal expansion coefficient for SBN is reported only for compositions x=0.35-0.59 and temperature range 20-50 °C, and for x=0.5 composition up to 500 °C. Here, X-ray diffraction of $Sr_{0.4}Ba_{0.6}Nb_2O_6$ (SBN40), $Sr_{0.5}Ba_{0.5}Nb_2O_6$ (SBN50) and $Sr_{0.6}Ba_{0.4}Nb_2O_6$ (SBN60) is reported in the temperature range up to 930 °C. The thermal expansion is anisotropic, differing significantly for the *a* and *c* lattice parameters, and a larger variation in the thermal expansion of the *c* lattice parameters was observed as a function of composition. Above the Curie temperature, the thermal expansion coefficient is decreasing with increasing temperature and decreasing Sr content. Linear thermal expansion coefficients range from 11.45(5) to 7.90(3) · 10^{-6} K^{-1} for the *a* lattice parameter and 9.10(1) to 4.40(1) · 10^{-6} K^{-1} for the *c* lattice parameter depending on composition and temperature range.

Acknowledgement

Financial support from NTNU Norwegian University of Science and Technology is acknowledged. The Swiss-Norwegian beamlines (SNBL) at European Synchrotron Radiation Facility (ESRF) is acknowledged for the allocation of beamtime and help during the experimental acquisition.

Keywords

$Sr_xBa_{1-x}Nb_2O_6$ (SBN), thermal expansion coefficient, *in situ* X-ray diffraction

Abbreviations

$Sr_xBa_{1-x}Nb_2O_6$ (SBNx*10), tetragonal tungsten bronze (TTB), X-ray diffraction (XRD), Swiss-Norwegian beamlines (SNBL), European Synchrotron Radiation Facility (ESRF), atomic displacement parameter (ADP)

Introduction

Ferroelectric tetragonal tungsten bronze $Sr_xBa_{1-x}Nb_2O_6$ (SBN) has been widely studied for its electro-optic, dielectric, piezoelectric, and ferroelectric properties, including a relaxor behavior for high Sr contents (x>0.5)[1-5]. SBN has a tetragonal tungsten bronze (TTB) structure with the P4bm space group in the low temperature ferroelectric phase and the P4/mbm space group for the high

temperature paraelectric phase [6, 7]. The TTB structure consists of corner-sharing NbO_6 octahedra in a framework that creates three different channel types, pentagonal, square and triangular along the *c*-axis of the structure [8]. The cations are distributed on the five cation sites, A1, A2, B1, B2 and C, as illustrated in Figure 1. In the case of SBN, the Nb-ions occupy all B sites, the C sites are empty, the larger Ba-ions are assumed to only reside in the larger A2 sites, and the Sr-ions occupy a distribution of A1 and A2 sites. [9, 10] Only 5 of 6 A sites are occupied in SBN and vacancies can be found on both the A1 and A2 sites, making SBN an unfilled TTB structure, giving an inherent disorder and large chemical flexibility and tunability of properties [7, 11-13].

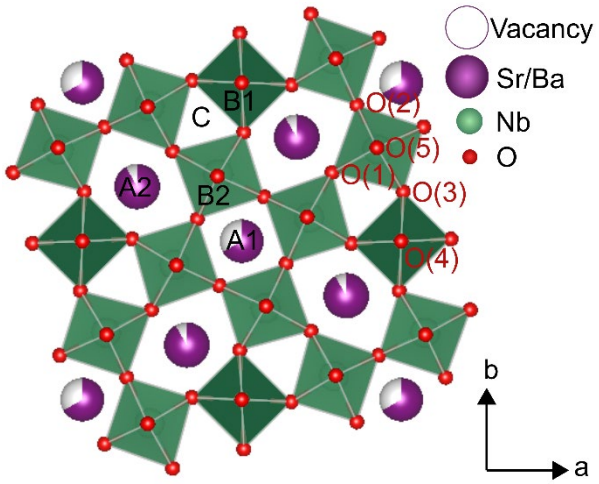

Figure 1: The tetragonal tungsten bronze (TTB) crystal structure of SBN projected along the c-axis. The different cation sites are marked by A1, A2, B1, B2, and C, while the anion sites are marked O(1)-O(5). The figure is adapted from [11] and uses the crystal structure as found by Podlozhenov et al. [10] and visualized by Vesta [14].

The ferroelectric to paraelectric phase transition is the only known phase transition for SBN[13]. In addition, an incommensurate modulation of the structure with tilted NbO_6 octahedra along the *c*-axis is found with single crystal diffraction [15] [16], but it is hardly visible and therefore often neglected in the powder diffraction [17]. SBN is a uniaxial ferroelectric with the polarization along the *c*-axis [1, 13]. A close to linear decrease in the phase transition temperature (Curie temperature, T_C) from 250 to 60 °C is reported with increasing x, i.e., Sr content, in the range 0.25-0.75 [1]. Further, the emergence of relaxor behavior with increasing x is also accompanied by a blurring or broadening of the phase transition over a wider temperature range which manifests as more gradual, rather than sudden change of the thermal expansion coefficient (α) close to T_C [18].

The thermal expansion of SBN has been studied for single crystals [2, 17-19], ceramics [20] and to some extent for thin films[21], in the temperature range from -258 to 500 °C. To the author's knowledge, no studies on the thermal behavior of SBN have been reported above 500 °C. The thermal expansion shows different behavior for the *a* and *c* lattice parameters of SBN. For the *a* lattice parameter, the thermal expansion is positive for all temperatures, and a nearly linear increase with temperature is observed in the range before and after the phase transition [2, 17-19]. At the phase transition, however, there is a change in the slope of the *a* lattice parameter vs temperature [18, 19]. For the *c* lattice parameter, a negative thermal expansion is observed until the phase transition with a tendency towards positive thermal expansion above the phase transition [17, 18, 21]. The negative thermal expansion and corresponding anisotropy below the phase transition have been coupled to the placement of the Nb-ions in the oxygen octahedra and Nb-ion thermal motion in the *a*-*b* plane. The Nb-O distance in the NbO_6 octahedra along the *c*-axis is non-uniform causing an off-centering of the Nb-ion and disorder in the chains. Further thermal motion of the Nb-ions

perpendicular to the O-Nb-O chain causes a reduction in the O-O separation along the *c*-axis which gives rise to the negative thermal expansion [2]. The overall change in cell volume of SBN is positive with increasing temperature [2]. Thermal expansion coefficients for SBN in the composition range x=0.35 to 0.59 have been reported to be between 12.57(34) and 13.42(21) · 10^{-6} K^{-1} along the *a*-axis and between -3.43(19) and -4.32(45) · 10^{-6} K^{-1} along the *c*-axis for single crystals in the temperature range 20-50 °C [18]. For SBN61 the linear part of the thermal expansion coefficient for the *a*-axis was reported to be 10(4) · 10^{-6} K^{-1} in the temperature range -258-27 °C [17]. Further, an average linear thermal expansion coefficient was measured by dilatometry to be 10.5(5) · 10^{-6} K^{-1} for SBN50 up to 500 °C [20].

Knowledge about the thermal expansion of SBN materials, also at higher temperatures, is important for crystal growth [2], design and fabrication of devices [18], use in composites with stress induced ferroelectric and magnetoelectric properties [22] and thin film synthesis due to the thermal mismatch between the film and the substrate giving thermal strain [21]. In this work, $Sr_{0.4}Ba_{0.6}Nb_2O_6$ (SBN40), $Sr_{0.5}Ba_{0.5}Nb_2O_6$ (SBN50) and $Sr_{0.6}Ba_{0.4}Nb_2O_6$ (SBN60) were studied by *in situ* synchrotron X-ray diffraction to reveal the phase transition and changes in the lattice parameters in the temperature range 25 to 930 °C. The work aims to improve the understanding of the high temperature, above 200 °C, behavior of SBN by providing quantitative values of the thermal expansion as a function of the composition. To the author's knowledge, no such values have been previously reported in the literature.

Materials and Methods

SBN40, SBN50 and SBN60 powders were produced by solid state synthesis, based on the work by Aamlid *et al.* [23]. $SrCO_3$ (Sigma Aldrich 99.9%), $BaCO_3$ (Sigma Aldrich 99.9%), and Nb_2O_5 (Sigma Aldrich 99.9%) were dried at 200 °C (>12 h) and mixed in stochiometric amounts in ethanol. The dried mixtures were further uniaxially pressed (30 MPa) and calcined at 1150, 1190 or 1240 °C for 24 h. Powders were crushed prior to use.

In situ X-ray diffraction measurements up to 930 °C were performed at BM01 (Swiss-Norwegian beamlines (SNBL), European Synchrotron Radiation Facility (ESRF), Grenoble), using a wavelength of 0.60546 Å, a beam size of 240x180 μm^2 and a 2M Pilatus detector (Dectris). The materials were mounted in 0.3 mm quartz capillaries and heated by a custom solid-state heater with a SiC head and Si_3N_4 resistive heat-cartridge [24]. Heating and cooling rates were 15 °C/min. Diffraction images were acquired with a 2θ range of 2.6-35°, 2 s exposure time and 20 ° rotation of the capillary. An approximate delay of 2-3 s between each frame gave an acquisition for every degree during heating. The temperature was monitored by a thermocouple and the corresponding material temperature was calibrated by a thermal expansion of silver standard. In addition to the temperature data, ambient temperature images with increased 2θ range (2.6-61°) and 10 s exposure time was acquired before heating to enable full Rietveld refinements. A LaB_6 NIST SRM 660a standard was used to determine detector position and beam characteristics for refinement of the data. The data was integrated using the Bubble software [25] and Rietveld refinement was performed in TOPAS [26].

The background in the diffractograms was fitted with a polynomial, a macro, developed by Chernyshov *et al.* [27], accounted for the beam and detector-related line broadening and the zero error was refined to account for any sample/beam displacements. A single phase SBN with either the space group P4bm (before ferroelectric phase transition) or P4/mbm (after ferroelectric transition) was used to calculate the lattice parameters and strain at different temperatures. The starting parameters for the atom positions were taken from Carrio *et al*. [9] for the P4bm space group and further refined using the ambient temperature data for each composition. The atom positions and

displacement parameters of Sr, Ba and Nb atoms were refined, while the oxygen atoms were kept fixed from the reference. For the P4/mbm space group the same atom placements as in the P4bm space group were used, except for the *z*-positions of all atoms (Sr, Ba, Nb and O) which were fixed to either 0 or 0.5 to account for the mirror plane.

To refine the temperature dependent data, an automatic process with iterative refinements was utilized in TOPAS launch mode. The data was refined twice, first with the P4bm space group, starting from ambient temperature, then with the P4/mbm space group starting from the maximum temperature. Lattice parameters, strain, Sr occupancy and atomic displacement parameters (ADPs) of Sr, Ba and Nb atoms were extracted, while the atom positions of the Sr, Ba and Nb atoms were fixed to the values found at ambient temperature for both space groups. A manual fit was performed on the starting frame and then the result from the previous frame was used as the starting point of the next frame. The phase transition for each material was determined from the minimum of the *c* lattice parameter fitted to a 6^{th} order polynomial [18]. Correspondingly the results from the P4bm space group were used below this temperature and the results from the P4/mbm space group were used above.

The thermal expansion coefficients were calculated using a 2^{nd} order polynomial regression in the Thermal Expansion Visualizing software [28] and an 1^{th} order polynomial regression in the Pascal software [29].

Results

The ferroelectric phase transition in SBN is not accompanied by any significant changes in the diffraction patterns. A minimum in the *c* lattice parameter is the most distinguished feature of the transition[19]. The overall results showed that heating of SBN40 (Figure 2) followed the expected behavior with no significant changes in the diffraction pattern, except the shifts in 2θ caused by thermal expansion. SBN50 and SBN60 demonstrated similar behavior, shown in Figure S1 in Supporting information.

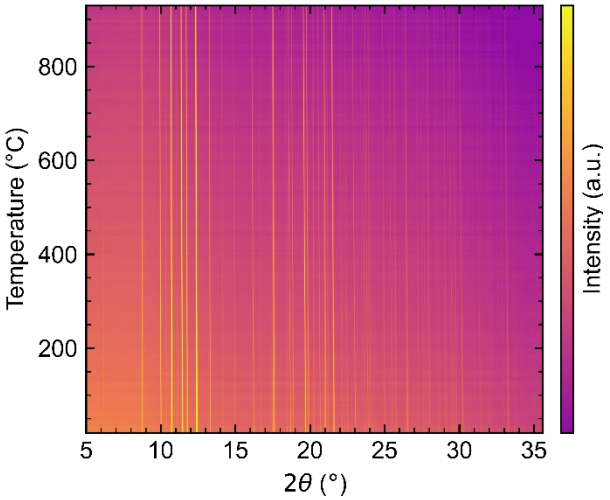

Figure 2: Temperature development of the X-ray diffraction pattern of $Sr_{0.4}Ba_{0.6}Nb_2O_6$ (SBN40) during heating to 930 °C.

The ambient temperature structural parameters obtained by Rietveld refinement of the SBN40-60 diffractograms are given in Table 1. The diffractograms together with the fitted data are shown in Figure S2 in Supporting information. The refinements gave a good fit with R_{wp} values in the range of 0.40-0.60 % and corresponding goodness of fit (GOF) of 1.02-1.26. Further, the obtained values are

seen to be close to reported literature values, although the *a* lattice parameter is slightly higher than most reported values, while the *c* lattice parameter is slightly smaller [9, 10, 21]. It should also be noted that little spontaneous strain is observed.

Table 1: Structural parameters for the P4bm phase of SBN as obtained from Rietveld refinements of the ambient temperature data and used as starting parameters for the temperature refinements with the P4bm space group.

Material	SBN40	SBN50	SBN60
a lattice parameter (Å)	12.4837(3)	12.4806(3)	12.4754(3)
(literature)	12.4828[10]	12.4852(6)[10] (SBN48)	12.4603(3)[9] (SBN61)
c lattice parameter (Å)	3.9618(1)	3.9506(1)	3.94034(1)
(literature)	3.9648[10]	3.9566(5)[10] (SBN48)	3.9315(2)[9] (SBN61)
e0	0.00035(1)	0.00026(1)	0.00018(1)
Occupancy Ba A2	0.75	0.625	0.5
Occupancy Sr A2	0.165(4)	0.267(4)	0.376(3)
Occupancy Sr A1	0.670(7)	0.716(7)	0.749(7)
$A1_z$	0.5034(44)	0.5060(49)	0.4991(49)
$A2_x$	0.1722(2)	0.1723(2)	0.1721(2)
$A2_y$	0.6722(2)	0.6723(2)	0.6721(2)
$A2_z$	0.4860(30)	0.4899(37)	0.5119(31)
U_{iso} A1	0.0077(14)	0.0122(13)	0.0231(13)
U_{iso} A2	0.0232(8)	0.0257(8)	0.0298(8)
$Nb1_z$	0.0314(28)	0.0268(31)	-0.0094(30)
$Nb2_x$	0.0748(1)	0.0749(1)	0.0749(1)
$Nb2_y$	0.2111(1)	0.2115(1)	0.2113(1)
$Nb2_z$	0.0005(25)	-0.0037(27)	0.0194(18)
U_{iso} Nb1	0.0057(9)	0.0100(9)	0.0148(9)
U_{iso} Nb2	0.0092(4)	0.0108(4)	0.0152(4)
R_{wp} (%)	0.59	0.60	0.40
GOF	1.02	1.03	1.26

The thermal evolution of the refined lattice parameters and unit cell volume for the SBN40-60 materials are presented in Figure 3. A monotonical increase in the *a* lattice parameters was observed, as shown in Figure 3 a). Around T_C, marked by the vertical lines in Figure 3, there is a small change in the slope of the *a* lattice parameter. For the *c* lattice parameter however, a clear change occurs at T_C. A minimum is observed at the phase transition temperature in accordance with literature [17, 18, 21], and the *c* lattice parameter has a negative thermal expansion below T_C. The unit cell volume (Figure 3 c)) however is dominated by the *a* lattice parameter and has a monotonic increase with temperature and a change in slope at the phase transition. The Currie temperature for SBN40, SBN50 and SBN60, respectively were estimated to 178, 140 and 105 °C based on the minimum value of the *c* lattice parameter. The estimated phase transition, based on the diffraction data, are considerably higher than T_C reported from dielectric spectroscopy of ceramics; ~140 [30]-175 [31] °C for SBN40, ~100 [30]-120 °C [20, 31] for SBN50 and ~70 [30]-80 °C [31] for SBN60. T_C reported by dielectric spectroscopy is considered to define the phase transition more precisely than from X-ray diffraction. The diffraction and dielectric data were collected for powder and ceramic samples and also with different temperature ramps so we cannot exclude the kinetic effects. We have however used T_C from the diffraction data in this work. T_C decreases with increasing Sr content in SBN, and the observed minimum in the *c* lattice parameter becomes broader, which is also accompanied by an increasing relaxor behavior of SBN with increasing Sr content [18].

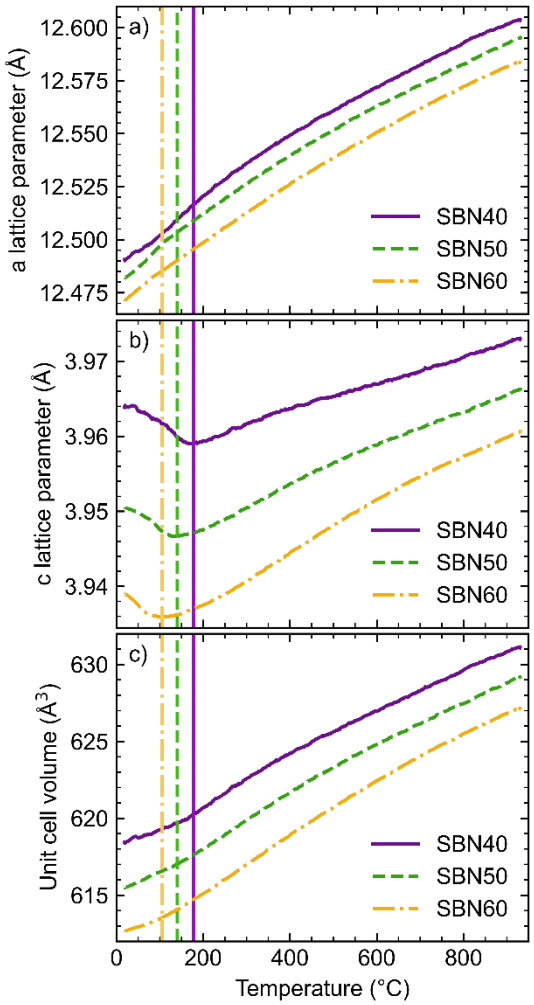

Figure 3: Evolution of the a (a)) and c (b)) lattice parameters, and unit cell volume (c)) as a function of temperature for SBN40-60 materials during heating. The Curie temperature for each material is marked by a colored vertical line.

The refined ADPs for the A2, A1, Nb1 and Nb2 sites, see Figure 4, show an approximately linear increase with temperature above T_C, except A1 which is linear until reaching a maximum around 550 °C. Across the phase transition, however, only the Nb2 site retains the linear increase while the remaining sites show an abrupt change or jump in the APDs at the phase transition. The jump in the Nb1 site is the most pronounced change and is previously reported in the literature [5]. The quality parameters of refinement (R_{wp} and GOF), and fitted parameters (zero error, strain and Sr occupancy) as a function of temperature are shown in Figure S3 in Supporting information. The refined structure for the first and last frame of the heating sequence are included in Supporting information, Figures S4 and S5. Generally, a reasonably good fit with a GOF below 2.2 for all frames was obtained.

The thermal expansion of SBN was determined from the heating data. The cooling data were not chosen due to the formation of crystalline quartz from the capillary at ~930 °C, which has diffraction lines overlapping with those from SBN. The thermal expansion was obtained separately from the data before and after T_C. A temperature range from 200 to 930 °C was selected for the data above T_C, to avoid any effects from the phase transition. The thermal expansion for both the *a* and *c* lattice parameters above 200 °C was fitted to a second order polynomial according to equation 1 using the Thermal Expansion Visualizing software [28]:

$$f(T) = p_2T^2 + p_1T + p_0 \quad (1)$$

where f stands for *a* or *c* unit cell dimensions, T is temperature and p_2, p_1 and p_0 are phenomenological constants.

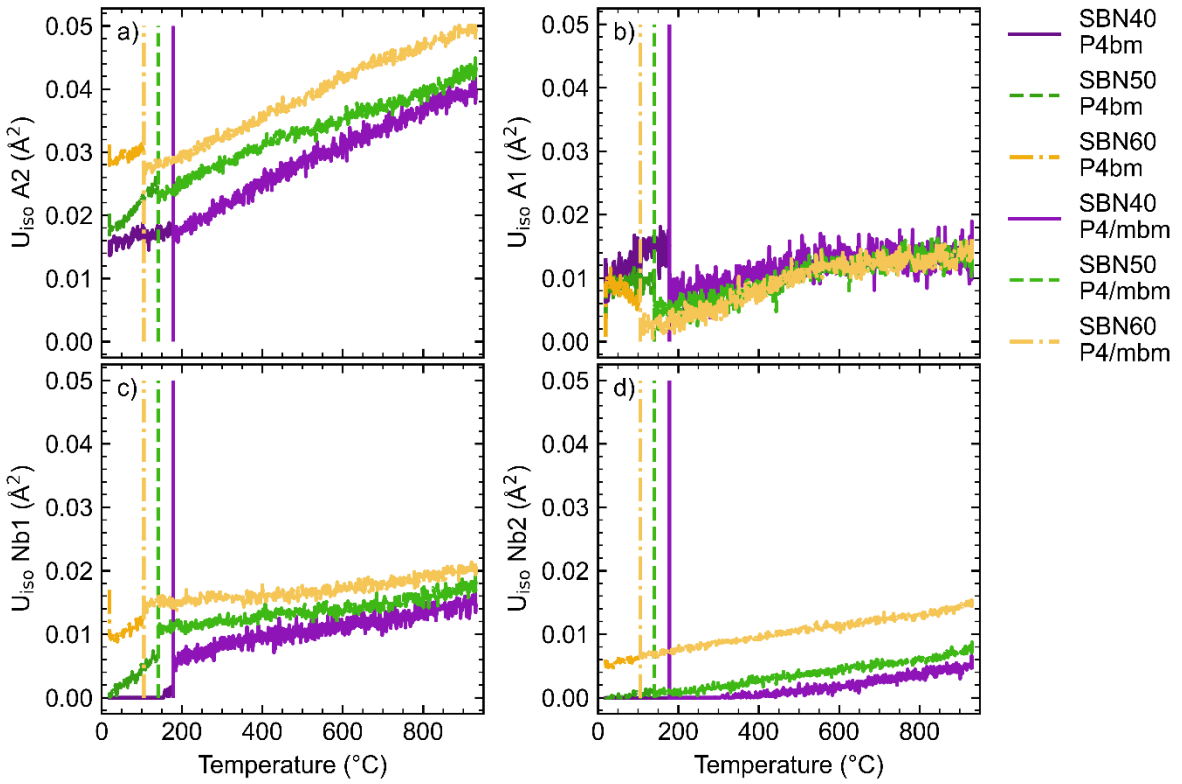

Figure 4: The atomic displacement parameters (ADPs) for the A2 (a)), A1 (b)), Nb1 (c)) and Nb2 (d)) sites obtained from Rietveld refinements of SBN40-60 in the temperature range 25-930 °C. The refined APDs are shown for the P4bm space group below the phase transition, marked by the vertical lines, and the P4/mbm space group above the transition (defined by the minimum in the c unit cell parameter).

The polynomial fit of the data is shown in Table S1 and plotted together with the lattice parameters in Figure S6 in Supporting information. The high R^2 values and close proximity of the fitted and experimental data show a good fit. The temperature dependence of the thermal expansion coefficients for the SBN40-60 materials is shown in Figure 5 a). In both crystallographic directions, the thermal expansion coefficient for the three materials decreases with increasing temperature. Figure 5 a) shows that the thermal expansion of the *a* lattice parameter behaves similarly for all three materials, while the *c* lattice parameter thermal expansion has a large variation showing an increasing thermal expansion with increasing Sr content. The crystallographic anisotropy along the *a* and *c* unit cell axes is composition and temperature dependent, as shown in Figure 5 b) where 3D

representations of the relative values of the thermal expansion coefficients in the two unique directions at selected temperatures are given.

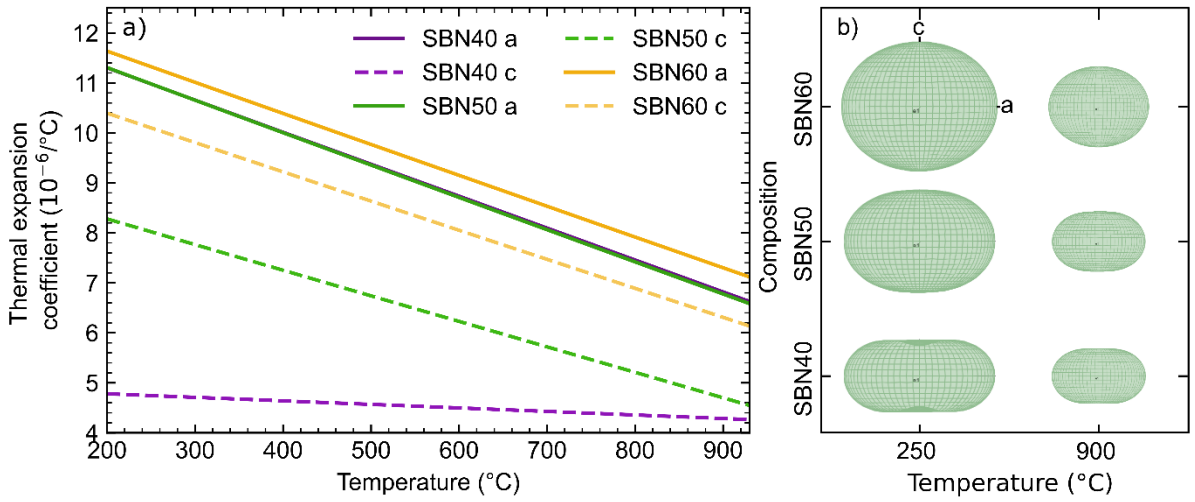

Figure 5: a) Thermal development of both the a and c lattice thermal expansion coefficients for the SBN40-60 materials. b) A 3D visualization of the thermal expansion coefficients for the SBN40-60 materials at selected temperatures, 250 and 900 °C, to show the change in isotropy with composition and temperature.

To obtain values for the linear thermal expansion coefficients, the thermal expansion was fitted by two linear regions intercepted at an intermediate temperature called T_i, which was individually determined for each composition to minimize R^2. The linear thermal expansion coefficients with errors as found with the software Pascal [29] are shown in Table 2. The values and trends of the coefficients correspond with the thermal expansion coefficients shown in Figure 5, except for an apparent decrease in the linear thermal expansion coefficients for the *a* lattice parameter with increasing Sr content. The decrease in coefficients is caused by a change in the temperature ranges considered in the calculation of the coefficients, given by T_i. Further, the decrease of thermal expansion coefficients with temperature is much stronger than the change with composition for the *a* lattice parameter, hence giving the apparent opposing trend with Sr content. The *c* lattice parameter on the other hand, have a strong composition dependence which dominated the temperature dependence and gives an increasing thermal expansion coefficient with increasing Sr content as observed in Figure 5. Table 2 also includes the linear thermal expansion coefficients in the low temperature region (25 °C - T_C) together with previously reported literature values [18]. A reasonable agreement between the data was found for the *a* lattice parameter coefficients in SBN40 and SBN60. For the *c* lattice parameter coefficients, however, a significantly larger negative thermal expansion coefficient is reported here compared to previously reported values.

*Table 2: Linear thermal expansion coefficients calculated using Pascal, for the a and c lattice parameters of SBN40, SBN50 and SBN60 in the temperature range 25-930 °C. Three separate temperature regions are considered; from 25 °C – T_C, from 200 °C to an intermediate temperature (T_i) and from T_i to 930 °C. Literature values from Paszkowski et al. [18] is included for the low temperature range and marked by *.*

			25 °C – T_C		200 °C – T_i		T_i - 930 °C	
Composition	T_C (°C)	T_i (°C)	α_a (10^{-6} K^{-1})	α_c (10^{-6} K^{-1})	α_a (10^{-6} K^{-1})	α_c (10^{-6} K^{-1})	α_a (10^{-6} K^{-1})	α_c (10^{-6} K^{-1})
SBN40	178	400	13.34(14)	-9.67(12)	11.45(5)	5.80(3)	8.31(2)	4.40(1)
			12.57(35)*	-3.66(11)*				
SBN50	140	480	15.31(9)	-9.86(15)	10.66(3)	7.81(2)	8.05(2)	5.69(1)

SBN51			13.26(12)*	-4.18(40)*				
SBN59			13.42(21)*	-4.32(45)*				
SBN60	105	660	13.25(9)	-10.04(37)	10.21(3)	9.10(1)	7.90(3)	6.60(2)

Discussion

The thermal expansion coefficient of SBN decreases with increasing temperature and differs along the *a* and *c* unit cell directions. The thermal expansion coefficients in the *a* direction are largest and increases slightly with increasing Sr content, see Figure 5. Along the *c* direction on the other hand a larger variation with Sr content is observed as previously reported [18], where the thermal expansion coefficient increases with increasing Sr content. Furthermore, the temperature dependence of the thermal expansion coefficient along the *c* direction changes with composition. It is interesting to note that both the magnitude and the temperature dependence of the thermal expansion along the polar *c* axis is correlated with an increasing relaxor behavior. The relaxor behavior is accompanied by a larger thermal expansion and a more temperature dependent thermal expansion coefficient. A structural explanation for the different variations can be found by considering the TTB structure and the tolerance factor introduced by Wakiya *et al.* [32] and further discussed by Zhu *et al.* [33] together with the refined ADPs.

The TTB crystal structure is highly anisotropic [32] with a repeating layering of the cations along the *c* lattice direction equal to the perovskite structure, while the *a* lattice parameter has a cation layering where the repeating distance is approximately three times larger than for the *c* lattice parameter. Along the *a* direction, see Figure 1, there are several A cation channels across the unit cell making the structure more flexible to accompany the changes posed by increased thermal motion and distortion due to compositional changes. Along the *c* direction, on the other hand, there is a single A cation site per unit cell making it more directly coupled to changes in the structure along this direction. The compositional changes in the crystal structure can be linked to the TTB tolerance factor [15, 33], using atomic radii from Shannon and Prewitt [34] and Zhu *et al.*[29] and the weighted average radii for Sr and Ba. A small decrease in the tolerance factor (1.009, 1.004, 0.9982) with increasing Sr content from x=0.40 to x=0.60 is observed. A decreasing tolerance factor in perovskites is coupled to the A cation being too small for its allocated site [35] and this coupling is expected to also hold for the TTBs especially for the A1 site as the coordination is the same [32]. When the tolerance factor decreases, the structure can distort to accompany this by tiling of the NbO_6 octahedra, creating a more zig-zag pattern of the O-Nb-O linkage [8]. Such an octahedron tiling is previously reported in SBN and linked to the incommensurate modulation [15] and a reduction in space group symmetry and doubling of the unit cell along the *c* direction [36]. Further, the Nb-O distance is reported to decrease with increasing Sr content [10]. No attempt has been done to model the tiling in the current work, as the space group was chosen to the higher symmetry aristotypes for the Rietveld refinements.

Within the quasiharmonic approximation, thermal expansion coefficients are expressed via components of elastic compliance tensor and Gruneisen parameters [37].

$$\alpha_i = \frac{C_\eta}{V}\sum_j S_{ij}^T \gamma_j \qquad (2)$$

Here (in Voight notations) α_i and γ_i are 6 component vectors of thermal expansion coefficients and Gruneisen parameters. S_{ij} stays for components of 4th rank elastic compliance tensor, C_η and V indicate heat capacity and volume. Here Gruneisen parameters are taken as an averaged over phonon spectrum of derivatives of vibrational frequencies with respect to deformations [37].

$$\gamma_i = \sum_n \frac{1}{\omega_n}\frac{\partial \omega_n}{\partial \epsilon_i} \quad (3)$$

For a tetragonal symmetry two thermal expansion coefficients are given by the following expression [38].

$$\alpha_a = \frac{C_\eta}{V}((S_{11} + S_{12})\gamma_a + S_{13}\gamma_c) \quad (4)$$

$$\alpha_c = \frac{C_\eta}{V}(2S_{13}\gamma_a + S_{33}\gamma_c) \quad (5)$$

According to Shorrocks et al. [39], the necessary elastic compliance components for SBN50 are $S_{11}+S_{12}$ = 3.9, S_{13}= -1.2, S_{33} = 9.3 (pm^2/N). Negative value for α_c in the ferroelectric phase requires positive γ_c>3.8 γ_a; this may serve as an indication of enhanced anharmonicity of phonons associated with distortion of the unit cell along *c* direction in the ferroelectric phase. The other sign of increased anharmonicity is given by atomic displacement parameters (ADPs) that are inversely proportional to the phonon frequencies, where some of the atoms show an increase of ADPs on cooling near transition temperature [40].

ADPs on heating is reported in Figure 4 and demonstrate that only the Nb2 ADP remains linear across the phase transition, in contrast to previously reported behavior [5]. The remaining ADPs (A1, A2, and Nb1) show a change in slope at the phase transition. Refinements using both space groups across the phase transition (Figure S7 in Supporting information) demonstrate that this is not an artifact of refinement due to the change of space group at the transition temperature. However, the abrupt jump in values at the transition temperature is linked to the phase transition associated with the space group change. The abrupt increase in Nb1 ADP is the largest feature observed and has previously been reported by Li *et al.* [5]. Li *et al.* which attributed the feature to domain fluctuation above the phase transition where the Nb1 atom continues to displace along the *c*-axis even at elevated temperatures. Further, Li *et al.* also reported a decrease in the Nb1 ADP until a temperature of about 500 °C, this was observed in the anisotropic APDs and is therefore likely not visible in the isotropic parameters for this work.

Regarding the A site cation displacements, one can see that especially the A2 site shows more distortion at higher Sr content, possibly linked to the relaxor behavior. Increasing Sr content cause a decreasing average atom size at the site and correspondingly more space for movement and cation mixing. The APD behavior below and above the phase transition demonstrates a normal thermal behavior, which is disrupted upon the phase transition. SBN40 has the largest change in slope at the transition, while the relaxor SBN60 has almost no slope change. For the A1 site, the behavior is different with more atomic displacement present below the phase transition and a decrease in the displacement above the phase transition. Above the phase transition, a change in slope at about 550 °C is observed, indicating that another effect might be present at higher temperatures. One possible hypothesis is that the thermal motion at this point causes a complete reversal of the octahedral tiling leaving the same space for A1 cation displacement for all three compositions.

The negative thermal expansion coefficients below the phase transition have been attributed to a non-uniform O-Nb-O distance in the chain along the *c*-axis, where the perpendicular movement of these atoms causes the O-O separation to decrease along the *c*-axis [2]. Further, the thermal expansion changes to positive at the phase transition, indicating that other mechanisms become dominant. Here one explanation is that the increased A cation movement becomes dominant above the phase transition and hence influences the tiling of the octahedra by reversing the distortions. A larger capability for lattice changes, therefore, occurs in the more distorted Sr-rich relaxor materials.

Furthermore, one can observe that the anisotropy in thermal expansion coefficients is largest for the ferroelectric low Sr content material at low temperature where this mechanism is expected to have the least effect. The anisotropy gradually decreases with both increasing temperature and Sr content giving a more uniform thermal expansion. The proposed mechanism can further be linked to the observed ADPs for the A1 site. Here the saturation displacement at temperatures above 550 °C can be interpreted as a complete reversal of the octahedral tiling, leaving a similar space for atom motion for all compositions. However, below this temperature the displacement is reduced with increasing Sr content, contradictory to all the other APDs, indicating a limited space and more distorted structure for the relaxor SBN60, facilitating *c*-axis thermal expansion. To verify the proposed hypothesis, studies of the tiling pattern and thermal motion at higher temperatures are needed.

A comparison between this work's low temperature thermal expansion coefficient and data from Paszkowski *et al.* [18], see Table 2, reveals a reasonable agreement for the *a* lattice parameter for SBN40 and SBN60, while the remaining values are significantly larger in absolute value. The deviation is expected to be caused by the difference in temperature interval considered, 25 °C - T_C vs 293-323K (20-50 °C) [18]. The larger temperature range offers better averaging but also includes non-linear behavior close to the phase transitions, see Figure 3, making the values less reliable compared to low temperature data. Ideally, a larger temperature range well below T_C should be used, but as the focus of this paper is high temperature data no such measurements were performed. The low temperature data is included to give a comparison with available literature values and show a reasonable agreement despite the deviations discussed. Especially the *c* lattice parameters show non-linear behavior below the phase transition, with an increased negative slope close to the phase transition giving rise to the enlarged negative thermal expansion coefficient reported. Further, a small non-linearity with an increased positive slope close to the phase transition is observed for the *a* lattice parameter for SBN50, giving a similar explanation for the increased value reported. For the *a* lattice parameters of SBN40 and SBN60, see Figure 3, a mostly linear behavior is observed below the phase transition.

Finally, the thermal behavior is important to fully understand a material system and for several different applications. Examples of areas where knowledge of the thermal expansion is important includes; Crystal growth [2], where the thermal expansion can affect the strain in the materials, design and fabrication of devices [18], where several heating cycles with different thermal expansions between the materials are critical, in composites, where the stress affects the functional properties of the material [22] and thin films synthesis to be able to predict the thermal strain in the films imposed by the substrate [21].

Conclusion

The crystal structure of $Sr_{0.4}Ba_{0.6}Nb_2O_6$ (SBN40), $Sr_{0.5}Ba_{0.5}Nb_2O_6$ (SBN50) and $Sr_{0.6}Ba_{0.4}Nb_2O_6$ (SBN60) were characterized by *in situ* X-ray diffraction of ceramic powders in the temperature range 25-930 °C. The thermal expansion obtained from the refined diffraction data varied slightly with composition for the *a* lattice parameter, while the *c* lattice parameters showed a large composition dependence. The composition dependence was linked to the structure and the tolerance factor of tetragonal tungsten bronzes crystal structure. Below the phase transition the reported linear thermal expansion coefficients is positive for the *a* lattice parameter and negative for the *c* lattice parameter as expected due to the ferroelectric transition. Both thermal expansivity and atomic displacement parameters indicate an increase of anharmonicity and softening of phonons on heating towards the ferroelectric to paraelectric phase transition. Above the phase transition the

thermal expansion coefficient is positive for both lattice parameters and it generally decrease with increasing temperature and decreasing Sr content. Linear thermal expansion coefficients range from 11.45(5) to 7.90(3) · 10^{-6} K^{-1} for the *a* lattice parameter and 9.10(1) to 4.40(1) · 10^{-6} K^{-1} for the *c* lattice parameter depending on composition and temperature range.

References

1. Neurgaonkar, R.R., et al., *Tungsten bronze $Sr_{1-x}Ba_xNb_2O_6$: A case history of versatility.* Ferroelectrics, 1988. **87**(1): p. 167-179.
2. Qadri, S.B., et al., *Anisotropic thermal expansion of strontium barium niobate.* Applied Physics Letters, 2005. **86**(25): p. 251914.
3. Lukasiewicz, T., et al., *Strontium barium niobate single crystals, growth and ferroelectric properties.* Journal of Crystal Growth, 2008. **310**: p. 1464-1469.
4. Shvartsman, V.V. and D.C. Lupascu, *Lead-Free Relaxor Ferroelectrics.* Journal of the American Ceramic Society, 2012. **95**(1): p. 1-26.
5. Li, C., et al., *Long-Range and Local Structure of $Sr_xBa_{1-x}Nb_2O_6$ (x = 0.33 and 0.67) across the Ferroelectric-Relaxor Transition.* Chemistry of Materials, 2020. **32**(5): p. 1844-1853.
6. Olsen, G.H., S.M. Selbach, and T. Grande, *On the energetics of cation ordering in tungsten-bronze-type oxides.* Physical Chemistry Chemical Physics, 2015. **17**(45): p. 30343-30351.
7. Jamieson, P.B., S.C. Abrahams, and J.L. Bernstein, *Ferroelectric Tungsten Bronze-Type Crystal Structures. I. Barium Strontium Niobate $Ba_{0.27}Sr_{0.75}Nb_2O_{5.78}$.* The Journal of Chemical Physics, 1968. **48**(11): p. 5048-5057.
8. West, A.R., *Solid State Chemistry and its Applications*. 2014: Wiley.
9. Carrio, J.G., et al., *Structure Refinement of (Sr,Ba)Nb_2O_6 Ceramic Powder from Neutron and X-Rays Diffraction Data.* Materials Research, 2002. **5**: p. 57-62.
10. Podlozhenov, S., et al., *Structure of strontium barium niobate $Sr_xBa_{1-x}Nb_2O_6$ (SBN) in the composition range 0.32 <= x <= 0.82.* Acta Crystallographica Section B, 2006. **62**(6): p. 960-965.
11. Paściak, M., et al., *Local structure of relaxor ferroelectric $Sr_xBa_{1-x}Nb_2O_6$ from a pair distribution function analysis.* Physical Review B, 2019. **99**(10).
12. Kleemann, W., *The relaxor enigma - charge disorder and random fields in ferroelectrics.* Journal of Materials Science, 2006. **41**(1): p. 129-136.
13. Oliver, J.R., R.R. Neurgaonkar, and L.E. Cross, *A thermodynamic phenomenology for ferroelectric tungsten bronze $Sr_{0.6}Ba_{0.4}Nb_2O_6$ (SBN:60).* Journal of Applied Physics, 1988. **64**(1): p. 37-47.
14. Momma, K. and F. Izumi, *VESTA 3 for three-dimensional visualization of crystal, volumetric and morphology data.* Journal of Applied Crystallography, 2011. **44**(6): p. 1272-1276.
15. Woike, T., et al., *The modulated structure of $Ba_{0.39}Sr_{0.61}Nb_2O_6$. I. Harmonic solution.* Acta Crystallographica Section B, 2003. **59**(1): p. 28-35.
16. Krayzman, V., et al., *Incommensurate Modulation and Competing Ferroelectric/Antiferroelectric Modes in Tetragonal Tungsten Bronzes.* Chemistry of Materials, 2022. **34**(22): p. 9989-10002.
17. Schefer, J., et al., *Structural properties of $Sr_{0.61}Ba_{0.39}Nb_2O_6$ in the temperature range 10–500 K investigated by high-resolution neutron powder diffraction and specific heat measurements.* Physical Review B, 2006. **74**(13).
18. Paszkowski, R., K. Wokulska, and J. Dec, *Thermal expansion coefficients of strontium - barium niobate single crystals in the vicinity of the phase transition point.* Crystal Research and Technology, 2017. **52**(8): p. 1600368.
19. Qadri, S.B., et al., *Phase transition in $Sr_{0.75}Ba_{0.25}NbO_3$ near the Curie temperature.* Applied Physics Letters, 2006. **89**(22): p. 222911.

20. Köferstein, R., F. Oehler, and S.G. Ebbinghaus, *Investigations of nano-crystalline $Sr_{0.5}Ba_{0.5}Nb_2O_6$ and bulk ceramics synthesized by a polymerization method using PEG400.* Journal of the European Ceramic Society, 2019. **39**(4): p. 1156-1163.
21. Pavlenko, A.V., et al., *Structural Characteristics of Thin $Sr_{0.5}Ba_{0.5}Nb_2O_6$ Films in the Temperature Range 20–500°C.* Inorganic Materials, 2020. **56**(11): p. 1188-1192.
22. Jigajeni, S.R., et al., *Dielectric, magnetoelectric and magnetodielectric properties in CMFO-SBN composites.* Ceramics International, 2013. **39**(3): p. 2331-2341.
23. Aamlid, S.S., S.M. Selbach, and T. Grande, *The Effect of Cation Disorder on Ferroelectric Properties of $Sr_xBa_{1-x}Nb_2O_6$ Tungsten Bronzes.* Materials, 2019. **12**(7): p. 1156.
24. Marshall, K.P., et al., *A new high temperature, high heating rate, low axial gradient capillary heater.* Journal of Synchrotron Radiation, 2023. **30**(1).
25. Dyadkin, V., et al., *A new multipurpose diffractometer PILATUS@SNBL.* Journal of Synchrotron Radiation, 2016. **23**(3): p. 825-829.
26. Evans, J.S.O., *Advanced Input Files & Parametric Quantitative Analysis Using Topas.* Materials Science Forum, 2010. **650**: p. 1-9.
27. Chernyshov, D., et al., *On the resolution function for powder diffraction with area detectors.* Acta Crystallographica Section A, 2021. **77**(5): p. 497-505.
28. Langreiter, T. and V. Kahlenberg, *TEV—A Program for the Determination of the Thermal Expansion Tensor from Diffraction Data.* Crystals, 2015. **5**(1): p. 143-153.
29. Cliffe, M.J. and A.L. Goodwin, *PASCal: a principal axis strain calculator for thermal expansion and compressibility determination.* Journal of Applied Crystallography, 2012. **45**(6): p. 1321-1329.
30. Zhao, Y., et al., *Relaxor transition and properties of Mn-doped $Sr_xBa_{1-x}Nb_2O_6$ ferroelectric ceramics.* Ceramics International, 2016. **42**(15): p. 16697-16702.
31. Kang, B. and G.-T. Joo, *Dielectric Properties of $Sr_xBa_{1-x}Nb_2O_6$ Ceramics and Single Crystals.* Japanese Journal of Applied Physics, 2006. **45**(3L): p. L245.
32. Wakiya, N., et al., *Synthesis and dielectric properties of $Ba_{1-x}R_{2x/3}Nb_2O_6$ (R: rare earth) with tetragonal tungsten bronze structure.* Journal of the European Ceramic Society, 1999. **19**(6): p. 1071-1075.
33. Zhu, X., et al., *A Crystal-Chemical Framework for Relaxor versus Normal Ferroelectric Behavior in Tetragonal Tungsten Bronzes.* Chemistry of Materials, 2015. **27**(9): p. 3250-3261.
34. Shannon, R.D. and C.T. Prewitt, *Effective ionic radii in oxides and fluorides.* Acta Crystallographica Section B, 1969. **25**(5): p. 925-946.
35. Goldschmidt, V.M., *Die Gesetze der Krystallochemie.* Naturwissenschaften, 1926. **14**(21): p. 477-485.
36. Campbell, B., et al., *An algebraic approach to cooperative rotations in networks of interconnected rigid units.* Acta Crystallographica Section A, 2018. **74**(5): p. 408-424.
37. Sammis, C., *Thermodynamics of crystals by D. C. Wallace.* Acta Crystallographica Section A, 1973. **29**(5): p. 582-583.
38. Ritz, E.T., S.J. Li, and N.A. Benedek, *Thermal expansion in insulating solids from first principles.* Journal of Applied Physics, 2019. **126**(17).
39. Shorrocks, N.M., R.W. Whatmore, and S.T. Liu, *The electro-elastic and SAW properties of $Sr_{0.5}Ba_{0.5}Nb_2O_6$.* Journal of Physics D: Applied Physics, 1982. **15**(12): p. 2469-2481.
40. Willis, B.T.M. and A.W. Pryor, *Thermal vibrations in crystallography / B. T. M. Willis, A. W. Pryor*. 1975, London ;: Cambridge University Press.